EAI Endorsed Transactions
on Energy Web
Research Article EAI.EU

Uncertainty Pattern Recognition of Multi-Type Renewable Power Plants and the Coupling Mechanism with Multi-Level Voltage Sensitivity

Xiaoyu Luo[1,*], Li Xiong[2], Lili Lv[1], Zhi Zhang[1], Yulong Li[1], Mingzhao Meng[1], Lei Zhuo[1], Xin Zhou[1]

[1]Laibin Power Supply Bureau of Guangxi Power Grid Co., Ltd., Laibin, 546100, China
[2]Power Dispatch Control Center of Guangxi Power Grid Co., Ltd., Nanning, 530000, China

Abstract

With high penetrations of renewable power plants, increased output volatility and uncertainty exacerbate local voltage-stability risks. Targeting heterogeneous renewable facilities, this paper proposes an integrated analysis framework that couples deep feature disentanglement, joint forecasting, and multi-level voltage sensitivity. First, using event logs as the driver, we combine variational mode decomposition (VMD) with a residual convolutional autoencoder (Res-CAE) to extract multi-band disturbance modes from power time series. An adversarial mechanism is then employed to disentangle meteorological disturbances from device-driven behaviors, yielding canonical uncertainty labels dominated by high-/mid-frequency components. Next, a spatio-temporal attention–driven multi-task sequence model is designed to jointly forecast active/reactive power and nodal voltage, providing stable inputs for subsequent sensitivity assessment. Finally, dynamic voltage sensitivity is estimated via sliding-window regression, and the disturbance–response chain and its propagation scope are quantified across local, dynamic, and system-level tiers. Event-driven simulations on the SoCal 28-Bus benchmark indicate that, under high- and mid-frequency dominated scenarios, dynamic voltage sensitivity increases by approximately 58.3% relative to low-volatility regimes, revealing a nonlinear transition by which renewable uncertainty is amplified through multi-frequency modes toward critical nodes. The proposed paradigm offers a transferable pathway for modeling and predicting complex source–network coupling in renewable-dominated power systems and provides data support for proactive voltage-control strategy design.

Keywords: renewable power plant, uncertainty modeling, joint forecasting, spatio-temporal attention, voltage sensitivity, feature disentanglement.

Received on 06 September 2025, accepted on 21 December 2025, published on 14 April 2026

doi: 10.4108/ew.12177

1. Introduction

With growing renewable integration, the rising shares of wind and photovoltaic (PV) plants introduce pronounced output volatility and uncertainty, tightening requirements on local voltage stability. High penetration makes voltage responses strongly time-varying, nonlinear, and multi-dimensionally coupled, limiting the effectiveness of conventional voltage-control methods based on linearization and static assessment. Stochastic power disturbances can further propagate through complex network paths and reach critical nodes, risking severe voltage deviations or instability [1–2].

*Corresponding author. Email: 16676676716@163.com

Uncertainty in renewable generation mainly stems from meteorological variability, heterogeneous device control, and forecasting errors [3–4]. Identifying these sources and tracing their propagation is essential for proactive regulation. Voltage sensitivity has thus gained attention as a key descriptor of disturbance–response coupling [5–6], yet static sensitivity models based on linearized power flow cannot capture dynamic mechanisms under high renewable penetration.

Recent work has used copulas, affine arithmetic, generative adversarial networks, and deep reinforcement learning to construct multi-dimensional uncertainty scenarios [3, 7], and probabilistic modeling, temporal convolution, and graph-based learning to enhance voltage forecasting and sensitivity analysis [5, 8, 9]. However, important gaps remain: (1) the lack of an end-to-end model linking power disturbances to voltage responses; (2) insufficient quantification of hierarchical voltage sensitivity and its nonlinear transitions; and (3) inadequate disentanglement of variability across heterogeneous renewable plants [10].

To address these issues, this study targets high-volatility conditions and proposes an integrated paradigm—feature disentanglement → joint forecasting → multi-level sensitivity—to characterize dynamic source–network interactions. The contributions are:

(1) Pattern recognition → sensitivity mechanism: A VMD–Res-CAE–adversarial framework extracts multi-frequency modes and separable representations. Using a unified event timeline, we construct local, dynamic, and system-level sensitivities, and verify consistency between reference sensitivities (small-signal/numerical Jacobian) and dynamic estimates (sliding-window regression), including threshold-τ analyses.

(2) Joint forecasting → interpretable indicators: A spatio-temporal attention multi-task model (STAN) jointly forecasts P/Q/V and outperforms LSTM/GRU/CNN-LSTM. Linking forecasts with modal features and sensitivities yields physically meaningful indicators such as prediction-error bands, sensitivity-peak persistence, and threshold-exceeding node proportions. Ablation and same-domain robustness tests confirm performance gains.

Event-driven verification is conducted on the SoCal 28-Bus system using multiple event windows and temporal rolling analyses. Broader engineering deployment will require additional validation across sites and longer event logs, as voltage trajectories are simulation-based and time-aligned to actual events. Limitations include reliance on simulated voltages, limited treatment of topological and frequency-domain variations, and demonstration on a single high-volatility plant. Future work will pursue multi-plant analysis, response-path visualization, and improved cross-system adaptability via data enrichment and knowledge transfer.

2. Related Research

2.1. Methods for Analyzing Output Characteristics of High-Variability Renewable Plants

Wind and photovoltaic (PV) outputs are shaped by meteorological variability, equipment states, and operating modes, leading to strong multi-scale volatility and spatial correlation [11–13]. Their joint behavior can be described by the joint density function:

$$f_{P_w,P_s}(p_w,p_s)=\frac{\partial^2}{\partial p_w \partial p_s}F_{P_w,P_s}(p_w,p_s) \quad (1)$$

which captures wind–solar correlation and complementarity. Dynamic complementarity is further reflected in the lagged cross-correlation coefficient [14]:

$$\rho_{ws}(\tau)=\frac{E\left[\left(P_w(t)-\mu_w\right)\left(P_s(t+\tau)-\mu_s\right)\right]}{\sigma_w\sigma_s} \quad (2)$$

However, such analyses rely on stationarity assumptions and mainly reflect linear dependence, limiting their ability to describe nonlinear coupling and multi–time-scale interactions under sudden disturbances or rapidly changing meteorological conditions.

2.2. Propagation Mechanism from Power Fluctuations to Voltage Responses

In power systems, power disturbances propagate through network impedances and topology, affecting voltages at both neighboring and remote nodes. To first order, this can be represented by the voltage–power sensitivity matrix [15]:

$$\Delta V=S_{VP}\cdot\Delta P \quad (3)$$

where $\Delta V \in \mathbb{R}^N$ is the vector of nodal-voltage variations, $\Delta P \in \mathbb{R}^M$ is the vector of active-power injections, and $S_{VP}(i,j)=\frac{\partial V_i}{\partial P_j}$ denotes the influence of the active-power change at node j on the voltage at node i.

In uncertainty analysis, acceptable voltage ranges at each node can be formulated via probabilistic constraints [16, 17]:

$$\Pr\{V_i(t)\in[V_i^{\min},V_i^{\max}]|\mathrm{P}(t)\}\geq\alpha \quad (4)$$

where $[V_i^{\min},V_i^{\max}]$ is the admissible interval, α is the confidence level, and $P(t)$ denotes the system-wide power vector at time t.

The voltage stability margin can be defined as [18]:

$$\lambda=\min_{\Delta P}\{\|\Delta P\|_2 \mid \det(J(V,P+\Delta P))=0\} \quad (5)$$

where J is the power-flow Jacobian and $\|\cdot\|_2$ is the Euclidean norm, quantifying the minimum perturbation distance from the operating point to the instability boundary.

Nonetheless, these formulations rely on linearization and steady-state assumptions, limiting their ability to capture time-varying propagation and multi-source disturbance interactions.

2.3. Definitions of Multi-Level Voltage Sensitivity

Voltage sensitivity characterizes how power disturbances propagate through the grid and is a key theoretical instrument in voltage-stability studies [5, 19, 20]. Under steady-state conditions, the inter-nodal sensitivity can be defined from the linear voltage–power relation via partial derivatives:

$$S_{VP}(i,j) = \frac{\partial V_i}{\partial P_j} \tag{6}$$

where S_{VP} is the static voltage–power sensitivity matrix, reflecting the coupling strength from a power change at node j to the voltage at node i.

Accounting for temporal variation in disturbances, the dynamic sensitivity is defined as:

$$S_D(i,j,t) = \frac{\mathrm{d}V_i(t)}{\mathrm{d}P_j(t)} \tag{7}$$

which describes the response speed and propagation direction of voltages under transient conditions.

At a more macroscopic level, a system-level sensitivity is often taken as a network-wide average [21]:

$$S_S = \frac{1}{NM}\sum_{i=1}^{N}\sum_{j=1}^{M}|S_{VP}(i,j)| \tag{8}$$

quantifying the overall susceptibility of the system to power perturbations. If disturbances are stochastic, one may further define an expected sensitivity:

$$\bar{S}(i,j) = \mathbb{E}_{\xi\sim D}\left[\frac{\partial V_i}{\partial P_j}\right] \tag{9}$$

where D denotes the distribution of power disturbances. The above multi-level definitions constitute the main theoretical basis for voltage-stability analysis.

Existing definitions generally depend on linearized models and static assumptions, lacking unified-timeline descriptions of dynamic behavior and cross-level interactions under fluctuating renewable outputs.

2.4. Formalizing Joint Modeling of Forecasting and Sensitivity

In renewable-dominated systems, forecasting and voltage-sensitivity regulation are increasingly viewed as coupled tasks [22,23]. Joint optimization typically takes the form [24]:

$$\min_{\theta,\mathrm{u}} \mathrm{L}_{\mathrm{pred}}(\mathrm{y},\hat{\mathrm{y}})+\beta\cdot\mathrm{L}_{\mathrm{sens}}(S(\mathrm{u})) \tag{10}$$

where $\hat{y} = f_\theta(x)$ denotes the forecasting model based on historical features such as power and voltage. The average squared difference between forecasts and actual observations is measured by the prediction loss function, represented by the symbol $\mathrm{L}_{\mathrm{pred}}$:

$$\mathrm{L}_{\mathrm{pred}}=\frac{1}{T}\sum_{t=1}^{T}\left\|\hat{\mathrm{y}}(t)-\mathrm{y}(t)\right\|_2^2 \tag{11}$$

In a similar vein, the sensitivity-related loss $\mathrm{L}_{\mathrm{sens}}$ is developed to assess the degree of alignment between the computed sensitivity matrix $S_L(i,j)$ and its reference distribution S_L^{target}:

$$\mathrm{L}_{\mathrm{sens}}=\frac{1}{NM}\sum_{i=1}^{N}\sum_{j=1}^{M}\left(S_L(i,j)-S_L^{\mathrm{target}}(i,j)\right)^2 \tag{12}$$

Here, β is a trade-off coefficient, and u represents control variables. Some studies further design a coordinated controller $\mathrm{u}=g_\phi(\hat{\mathrm{y}},S)$, which integrates forecasting results with sensitivity information to enable reactive-power adjustment and voltage optimization.

Although these frameworks offer a unified perspective on forecasting and regulation, most remain static and single-interval, giving limited attention to disturbance propagation or real-time adaptive responses. This leaves substantial room for advancing dynamic coordination mechanisms.

3. Research Methods

3.1. The chain of evidence and the overall framework

This study examines multi-level voltage sensitivity to assess how highly volatile renewable outputs affect voltage stability. The evidence chain follows: event anchoring → data alignment → feature/forecast supply → sensitivity evaluation → consistency verification → mechanistic interpretation. Switching and topology events are first used to synchronize temporal records and define disturbance scenarios. Feature extraction and time-series forecasting then generate stable inputs, where forecasting serves as an optional step to enhance reliability under missing or noisy measurements. Finally, local, dynamic, and system-wide sensitivities are quantified via sliding-window estimation and validated through consistency checks to reveal dominant disturbance–response pathways.

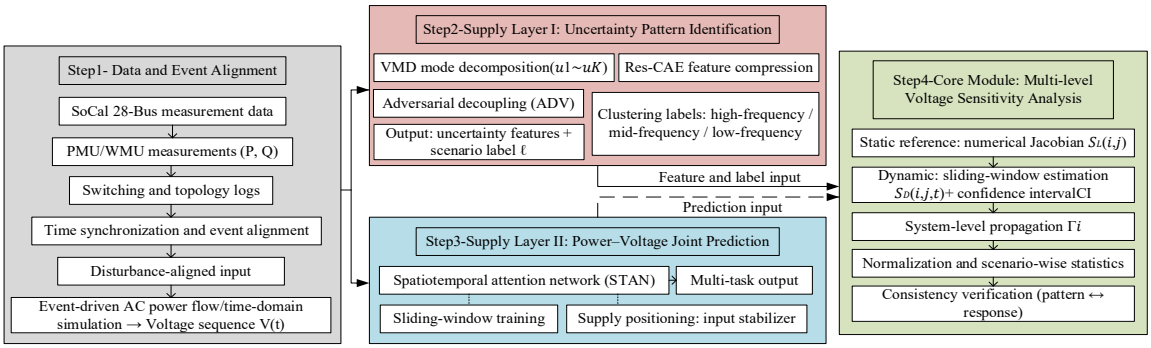

Figure 1. Overall framework and evidence chain

As shown in Figure 1, the framework consists of four modules:

(i) Dataset synchronization and scenario construction: A unified temporal reference is built by integrating measurements from the SoCal 28-Bus system with event and topology logs, enabling extraction of representative outage–reconnection sequences for analysis.

(ii) Uncertainty pattern recognition (supply layer): VMD and a Res-CAE extract multi-scale disturbance modes. Combined with adversarial feature disentanglement (ADV), the method separates meteorological- and device-driven components and labels canonical high-volatility patterns via clustering.

(iii) Joint power–voltage forecasting (supply layer): A spatio-temporal attention network (STAN) provides multi-task predictions to stabilize input signals for sensitivity analysis, particularly under data gaps or measurement noise.

(iv) Multi-level voltage sensitivity analysis (core module): Sliding-window regression estimates time-varying sensitivities for constructing local, dynamic, and system-level indicators. Pattern labels are linked to these indicators to characterize spatial propagation and disturbance intensity.

Within this framework, pattern recognition and forecasting serve purely as input layers, offering evidence and reliability metrics. The core innovations lie in the formulation, estimation, and multi-level representation of voltage sensitivities. Based on the architecture in Section 3.2, an event-driven simulation platform generates voltage trajectories for sensitivity analysis and subsequent mechanistic verification. Sections 3.3–3.4 detail the model configurations, and Section 3.5 defines the sensitivity indices and computation methods.

3.2. Data and Scenarios

This study uses multi-source measurements from the SoCal 28-Bus system [25], spanning 2023-08-01 to 2024-11-13 at 1 Hz, including PMU/WMU data and circuit-breaker/switch logs. Using operational alarms and recorded actions, timestamps are synchronized and the bus-17 islanding event on 2024-11-13 17:52:20 is segmented, producing matched pre- and post-event intervals that serve as temporal anchors for forecasting, pattern recognition, and sensitivity analysis.

Only power, status, and topology channels are used; no direct voltage measurements are available. Nodal voltage trajectories are therefore generated via an event-driven simulation platform based on the SoCal 28-Bus topology. Actual switching actions—including CB and SWMP opening/closing times—are translated into discrete disturbance events that dynamically modify network topology. The simulation incorporates line parameters, nominal bus voltages, load models, inverter Q–V control, and boundary conditions to ensure temporal consistency with the event logs at 1 Hz resolution.

A hybrid AC power-flow and time-domain scheme produces the voltage sequences. For each event-defined segment, steady-state power flow is solved to obtain a reference profile, after which a dynamic integrator (Δt = 0.01 s) updates system responses during disturbances. Simulated voltages are resampled to 1 Hz for alignment with recorded events. Loads follow the WECC composite model with dynamic (reactive compensation and induction motors) and static (ZIP) components. Inverter-side Q–V droop control (slope 2.5%/p.u., 200 ms delay) maintains voltage stability. A 100 MVA base and uniform boundary conditions are applied across simulations.

Dynamic sensitivities are estimated from sliding-window regression (τ = 60 s), while steady-state sensitivities are derived from the static Jacobian. Comparing these datasets verifies the physical consistency of modeled power–voltage relationships. All geographic identifiers and device labels are anonymized to satisfy confidentiality requirements, and all power and voltage values are expressed in per-unit (p.u.) terms.

3.3. Uncertainty Pattern Identification for a Single Plant

To characterize the time-varying behavior of renewable generation, we develop a recognition framework consisting

of preprocessing and alignment → multi-scale feature extraction → adversarial disentanglement → unsupervised clustering. The framework outputs physically interpretable scenario identifiers for downstream forecasting and sensitivity analysis.

(1) Preprocessing and data alignment (SoCal 28-Bus)

Circuit-breaker and switch-matrix logs offer millisecond-resolution device operations, while PMU/WMU channels provide power-flow measurements. All data are aligned to a unified 1 Hz timeline:

$$\mathcal{T} = \{t_0, t_1, \dots, t_n\} \tag{13}$$

with a binary process $c(t) \in \{0,1\}$marking events. Active-power signals are detrended with a moving average (default $\tau = 60$s):

$$\Delta P(t) = P_{\text{raw}}(t) - \text{MA}_\tau(t) \tag{14}$$

and all variables are converted to per-unit. Power series across devices are resampled and aligned on T. Bus_17 is treated as the main uncertainty source; multi-plant extensions can be handled in aggregated post-analysis.

(2) Multi-scale features via VMD and residual convolutional autoencoder (Res-CAE)

Variational mode decomposition (VMD) separates disturbances into Kintrinsic mode functions (IMFs):

$$\Delta P(t) = \sum_{k=1}^{K} u_k(t) \tag{15}$$

with $K \in \{4,5,6\}$ selected empirically or via AIC/MDL. Each IMF is encoded using a residual convolutional autoencoder:

$$z_k = f_{\text{enc}}(u_k(t); \theta_k), \hat{u}_k = f_{\text{dec}}(z_k; \phi_k) \tag{16}$$

optimized by:

$$\mathcal{L}_{\text{rec}} = \sum_{k=1}^{K} \|u_k - \hat{u}_k\|_2^2 + \gamma \sum_k \|z_k\|_1 + \eta \sum_k \|\nabla z_k\|_2^2 \tag{17}$$

where ∇z_kcontrols abrupt latent changes. Concatenating all latent vectors yields the global feature:

$$\mathrm{z} = [z_1, \dots, z_K]^\top \in \mathbb{R}^{d_z} \tag{18}$$

(3) Adversarial feature separation and pattern classification

To distinguish meteorological influences from device-driven disturbances, the latent vector $z$is projected into two subspaces:

$$\mathrm{z}_{\text{env}} = W_{\text{env}}\mathrm{z}, \mathrm{z}_{\text{dev}} = W_{\text{dev}}\mathrm{z} \tag{19}$$

where $W_{\text{env}}, W_{\text{dev}} \in \mathbb{R}^{d' \times d_z}$. A discriminator $D(\cdot)$enforces separation through:

$$\min_{f_{\text{enc}}, W_{\text{env}}, W_{\text{dev}}} \max_D \mathbb{E}[\log D(\mathbf{z}_{\text{env}})] + \mathbb{E}\left[\log\left(1 - D(\mathbf{z}_{\text{dev}})\right)\right] + \lambda_\perp \|W_{\text{env}}^\top W_{\text{dev}}\|_F^2 \tag{20}$$

Weak supervision (e.g., wind-speed or irradiance thresholds) can be added when available. Window-level pattern labels (high-, mid-, or low-frequency dominant) are obtained via a linear SVM or lightweight MLP, yielding posterior $p(l)$.

(4) Unsupervised clustering and prototypical-scenario generation

To capture unseen disturbance types, unsupervised clustering (K-means or DBSCAN) is applied:

$$c \in \{1, \dots, C\} \tag{21}$$

with C determined by density or silhouette metrics. The modal energy ratio evaluates frequency-band contributions:

$$E_k = \frac{\int_{\mathcal{W}} |u_k(t)|^2 \, \mathrm{d}t}{\sum_{j=1}^{K} \int_{\mathcal{W}} |u_j(t)|^2 \, \mathrm{d}t}, k = 1, \dots, K \tag{22}$$

where W is the analysis window. Each cluster yields a centroid $\bar{z}_c$and IMF prototypes $\{\bar{u}_k^{(c)}(t)\}$, which serve as canonical disturbance patterns and support scenario replay under different modal-dominant conditions.

3.4. Construction of a Joint Power–Voltage Forecasting Model

A spatio-temporal attention network (STAN) is developed for multi-task sequence prediction, integrating temporal and cross-variable attention to capture short-horizon dynamics during disturbances and stabilize the inputs for downstream sensitivity analysis. The model generates one-step forecasts of active/reactive power, and optionally short-term voltage extrapolation, using sliding-window samples on a unified 1 Hz timeline. The model design focuses on producing reliable feature representations rather than achieving optimal forecasting performance.

(1) Sequence architecture (Encoder–Attention–Decoder)

Given a window length T, the input at time t is:

$$X_t = [P_{t-T+1:t}, Q_{t-T+1:t}, Z_{t-T+1:t}] \in \mathbb{R}^{T \times d} \tag{23}$$

where Z contains optional exogenous features (e.g., meteorology or event flags). A two-layer GRU encodes temporal dependencies and produces latent states $\{h_1, \dots, h_T\}$.

Temporal attention highlights disturbance-relevant moments:

$$\alpha_\tau = \frac{\exp\left(q^\top \tanh\left(W_h h_\tau\right)\right)}{\sum_{i=1}^{T} \exp\left(q^\top \tanh\left(W_h h_i\right)\right)}, c = \sum_{\tau=1}^{T} \alpha_\tau h_\tau \tag{24}$$

where $W_h \in \mathbb{R}^{d_a \times d_h}$ and $q \in \mathbb{R}^{d_a}$ are trainable, d_a is the attention dimension, $\alpha_\tau \in (0,1)$ with $\sum_\tau \alpha_\tau = 1, c \in \mathbb{R}^{d_h}$ is the temporal context.

To capture cross-variable interactions, pooled variable representations are projected via $U \in \mathbb{R}^{d_v \times d}$and compared with query $c$to form variable-level attention coefficients β. The resulting variable-weighted context $\tilde{c}$is combined with $c$and decoded through a two-layer MLP to predict the next-step values. Default outputs are $\hat{P}_{t+1}$and $\hat{Q}_{t+1}$; an auxiliary branch produces $\hat{V}_{t+1}$ when alignment with simulated voltage trajectories (Section 3.2) is required.

(2) Multi-task objective and loss functions

The multi-task output at time t is:

$$\hat{y}_{t+1} = \left[\hat{P}_{t+1}, \hat{Q}_{t+1}, \left(\hat{V}_{t+1}\right)\right] = f_\theta(X_t) \tag{25}$$

where $f_\theta(\cdot)$ is the predictor with parameters θ, and $(\cdot)$ denotes the optional branch. The weighted MSE objective is:

$$\mathcal{L}_{\text{total}} = \lambda_P \mathcal{L}_P + \lambda_Q \mathcal{L}_Q + \lambda_V \mathcal{L}_V \tag{26}$$

$$\mathcal{L}_P = \frac{1}{N}\sum_{i=1}^{N}\left(\hat{P}_i - P_i\right)^2, \mathcal{L}_Q = \frac{1}{N}\sum_{i=1}^{N}\left(\hat{Q}_i - Q_i\right)^2, \mathcal{L}_V = \frac{1}{N}\sum_{i=1}^{N}\left(\hat{V}_i - V_{\text{sim},i}\right)^2 \quad (27)$$

where $\lambda_V \ll \lambda_P, \lambda_Q$ ensures the voltage branch acts as a regularizer rather than a dominant term. Dropout, layer normalization, and Adam optimization (learning rate η) are applied.

(3) Sliding-window training and sampling technique

On the 1 Hz axis, construct the training set:

$$\mathcal{S} = \{(X_t, \mathrm{y}_{t+1})\}_{t=T}^{T+L_{\text{tr}}-1} \quad (28)$$

with windows advancing by step s_{pred}. Typical settings are $T \in [60,300]$ s and $s_{\text{pred}} \in [1,10]$ s. Event-aligned samples receive higher weights $\omega > 1$ to enhance disturbance sensitivity. Early stopping is used based on validation loss.

(4) Inference and robustness design

During inference, sliding windows continuously produce $\{\hat{P}_{t+1}, \hat{Q}_{t+1}\}$ (and optional $\hat{V}_{t+1}$). Two useful methods are used to improve robustness under disturbance conditions:

1) Online detrending and adaptive scaling update normalization statistics and moving-average windows (as in Section 3.3) to address nonstationarity.

2) Temporal ensembling smooths predictions through exponentially decayed averaging across recent windows, reducing short-term noise prior to sensitivity analysis.

The forecasts serve as stabilized inputs for downstream evaluation rather than as final operational outputs.

3.5. Multi-Level Voltage Sensitivity Analysis Method

To characterize time-varying voltage responses driven by renewable-output fluctuations, we propose a multi-level framework combining a steady-state baseline, dynamic tracking, and system-level synthesis. Event and topology logs provide temporal anchors for synchronizing datasets. AC power-flow and time-domain simulations under predefined topologies generate nodal voltage trajectories at 1 Hz. Power injections are detrended using a moving-average filter (default $\tau = 60$s), and all variables use per-unit normalization. The static layer evaluates near–steady-state sensitivity through linearization, while the dynamic layer estimates evolving response patterns via sliding-window regression. Reporting both layers ensures physical consistency and avoids inference loops based solely on theoretical formulations.

(1) Static sensitivity (linearized power flow and numerical Jacobian)

Near a steady operating point, the small-signal linearization of the power-flow equations is:

$$\begin{bmatrix}\Delta P \\ \Delta Q\end{bmatrix} = \begin{bmatrix}J_{PP} & J_{PV} \\ J_{QP} & J_{QV}\end{bmatrix}\begin{bmatrix}\Delta\theta \\ \Delta\,|V|\end{bmatrix} \quad (29)$$

where $\Delta P, \Delta Q \in \mathbb{R}^n$ denote the nodal active/reactive injection perturbations, $\Delta\theta \in \mathbb{R}^n$ the phase-angle variations, and $\Delta\,|V| \in \mathbb{R}^n$ the changes in voltage magnitude; the system comprise n nodes, while $J_{PP}, J_{PV}, J_{QP}, J_{QV}$ represent the associated Jacobian submatrices. We define the static sensitivity of node j's voltage magnitude with respect to an active-power injection at node i as:

$$S_L(i,j) \triangleq \frac{\partial\,|V_j|}{\partial P_i} \quad (30)$$

We use central differences to numerically evaluate the derivative for a repeatable baseline. The corresponding power-flow solutions produce $|V_j|^{(+)}$ and $|V_j|^{(-)}$ when a perturbation of magnitude $\pm\delta P$ is applied at node i with $\delta = 10^{-3}$ p. u.. The approximation turns into:

$$S_L(i,j) \approx \frac{|V_j|^{(+)} - |V_j|^{(-)}}{2\delta} \quad (31)$$

This provides a repeatable steady-state reference for interpreting dynamic sensitivities.

(2) Dynamic sensitivity tracking (sliding-window regression with interval assessment)

Responses during disturbance periods are strongly time-varying. Let L(s) stand for the sliding-window span and s(s) for the step. We define the window on the 1 Hz time axis t:

$$\mathcal{W}_t = \{t - L + 1, \ldots, t\} \quad (32)$$

Create input-output pairs for each of these windows:

$$\{\Delta P_i(\tau), \Delta V_j(\tau)\}_{\tau \in \mathcal{W}_t} \quad (33)$$

and estimate the dynamic sensitivity via (ridge) linear regression:

$$\hat{S}_D(i,j,t) = \arg\min_{\beta} \sum_{\tau \in \mathcal{W}_t}\left(\Delta V_j(\tau) - \beta \Delta P_i(\tau)\right)^2 + \lambda\|\beta\|_2^2 \quad (34)$$

with regularization $\lambda = 10^{-3}$. Rolling by step $s$yields the trajectory $\{\hat{S}_D(i,j,t)\}$.

Multi-input extension. When including ΔQor exogenous variables, $X = [\Delta P_i, \Delta Q_i, Z] \in \mathbb{R}^{L\times d}$, and the coefficient associated with $\Delta P_i$is reported as $\hat{S}_D$.

Uncertainty quantification. Bootstrap resampling (default $B = 1000$) produces confidence intervals:

$$\mathrm{CI}_t = \left[\hat{S}_D^{\ell}(i,j,t), \hat{S}_D^{u}(i,j,t)\right] \quad (35)$$

where $\hat{S}_D^{\ell}$ and $\hat{S}_D^{u}$ are the 2.5% and 97.5% quantiles of $\{\hat{S}_D^{(b)}\}$ (adjustable confidence). Default parameters in this paper: L=120s, s=10s, λ=10^{-3}, B=1000, τ=60s.

Algorithm 1. Sliding-window estimation of dynamic voltage sensitivity (with confidence intervals)
Input: $\{P_t, Q_t, V_t\}$; window L; step s; regularization λ; resamples B.
for $t = L, L+s,$ ...do
1) Detrend using τ and construct X, y;
2) Solve $\hat{S}_D(i,j,t) = \arg\min_{\beta} \| y - X\beta \|_2^2 + \lambda \| \beta \|_2^2$;
3) Bootstrap B times to obtain CI_t;
end for

Output: $\{\hat{S}_D(i,j,t), \mathrm{CI}_t\}$.

(3) Hierarchical metrics of response intensity and propagation scope

We define the following indicators and align them to the event-aligned temporal axis to systematically characterize disturbance intensity and geographical reach.

1) Local Sensitivity.

Within the first-order neighborhood $N(i) \subseteq \{1, \ldots, n\}$ of node i:

$$S_L(i,j)|_{j\in N(i)} = \frac{\partial |V_j|}{\partial P_i} \tag{36}$$

to identify local weak spots and guide the prioritization of node-level interventions control. The set $N(i)$ is determined by network topology.

2) Temporal-Averaged Sensitivity (dynamic intensity).

Over $[t_0, t_0 + T^{'} - 1]$ with start t_0 and sample count $T^{'}$, the time average of $\hat{S}_D$ measures overall intensity during the disturbance period:

$$\bar{S}_D(i,j) = \frac{1}{T'} \sum_{t=t_0}^{t_0+T'-1} \hat{S}_D(i,j,t) \tag{37}$$

3) System Spread Index (system-level propagation).

Use an adaptive threshold ϵ: set ϵ to the 95th percentile of $|\hat{S}_D|$ over a user-specified pre-event baseline. During the disturbance period define:

$$R_i(t) = \{j : |\hat{S}_D(i,j,t)| > \epsilon\}, \Gamma_i = \frac{|\cup_t R_i(t)|}{n} \tag{38}$$

where node i acts as the initial disturbance point and $\Gamma_i \in [0,1]$ is the system coverage ratio. For cross-scenario comparisons, a fixed-threshold variant can also be adopted (e.g., scaling ϵ by a percentile of the steady-state baseline); both conventions are reported in the results.

(4) Normalization for cross-node comparison

Let $S = \{\hat{S}_D(i,j,t)\}$ represent the set of dynamic sensitivities for the scenario being studied, then use dimensionless standardization to eliminate scale variations between nodes and scenarios:

$$\tilde{S}_D(i,j,t) = \frac{\hat{S}_D(i,j,t) - \mu_S}{\sigma_S} \tag{39}$$

where $\mu_S$and $\sigma_S$are statistics computed over the scenario. Standardized trajectories facilitate clustering, trend analysis, and linkage with uncertainty-pattern labels. Reported quantities include $\hat{S}_D$, CI_t, $\bar{S}_D$, and Γ_i, supporting engineering interpretation and cross-scenario comparison.

4. Experiment

4.1. Data and Experimental Setup

(1) Dataset

The SoCal 28-Bus event-log dataset [25] spans 2023-08-01 to 2024-11-13 and records real operational states of the Southern California grid, including network configurations, parameter adjustments, and key device operations. The dataset contains:

1) netfile_changes.csv: initial topology configuration (2023-08-01T00:00:00) with no structural updates.

2) parameter_changes.csv: 16 timestamps of parameter or control changes.

3) Initial topology JSON file: bus/line attributes, rated voltages, phase configurations, device-state labels, line parameters, and area assignments.

4) 14 millisecond-resolution CB/SWMP state-sequence files documenting transitions between normally closed (NC) and open (NO) states.

As the public dataset does not include voltage measurements, nodal voltages are generated via an event-driven AC power-flow and time-domain co-simulation aligned to the 1 Hz timeline described in Section 3.2. The simulation integrates topology, line parameters, load models, and inverter Q–V control. Switching sequences from CB/SWMP logs drive topology changes, yielding physically consistent voltage trajectories for all disturbance windows. All voltage-related features, forecasts, and sensitivities in this study rely on this event-aligned simulation.

(2) Experimental settings and hyperparameters

Experimental focus. Using multi-source event alignment as a guide, we investigate two typical operating mode changes:

1) Ring reconfiguration (2023-11-26T09:27:10): coordinated closing of cb_134, cb_135, cb_138, cb_140, cb_142 and opening of cb_137 forms a local reliability-enhancing ring.

2) Islanding and reconfiguration of renewable plants is the main scenario this study looks at (2024-11-13).

Figure 2 illustrates the 2024-11-13 event sequence. At 17:52:20, breakers cb_121, cb_123, and swmp_17-2 open simultaneously, fully tripping the renewable plant. After 8 seconds, cb_128 closes to restore supply paths. The plant reconnects later when swmp_17-2, cb_121, and cb_123 close sequentially. This trip–reconfigure–restore cycle represents a typical high-volatility renewable disturbance and is the main analysis target.

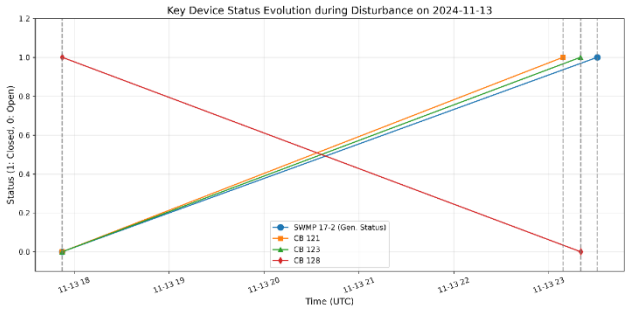

Figure 2. Evolution of key device states during the 2024-11-13 disturbance

The experiment centers on the 2024-11-13 window. PMU/WMU devices provide 1 Hz active and reactive power measurements, while voltage trajectories come from

the event-driven simulation in Section 3.2. Bus_25 is chosen as the target for voltage-response analysis, and Bus_17 serves as the renewable-station interconnection and primary disturbance source.

Training/testing split:

– Training set: 30 days of steady-state data (2024-10-14 to 2024-11-12).

– Evaluation set: entire day of 2024-11-13, with emphasis on the disturbance interval 17:52–23:31.

(3) Assessment Criteria

1) Forecasting effectiveness

Root Mean Square Error (RMSE)

$$\mathrm{RMSE}=\sqrt{\frac{1}{N}\sum_{i=1}^{N}\left(y_i-\hat{y}_i\right)^2} \tag{40}$$

Mean Absolute Error (MAE)

$$\mathrm{MAE}=\frac{1}{N}\sum_{i=1}^{N}\left|y_i-\hat{y}_i\right| \tag{41}$$

Coefficient of determination (R^2)

$$R^2=1-\frac{\sum_{i=1}^{N}\left(y_i-\hat{y}_i\right)^2}{\sum_{i=1}^{N}\left(y_i-\bar{y}\right)^2} \tag{42}$$

where $y_i$is the event-log reference, $\hat{y}_i$the prediction, $N$the number of samples, and $\bar{y}$their mean. Lower RMSE/MAE and higher R^2indicate better forecasting accuracy.

2) Voltage-sensitivity quantification

The dynamic voltage-sensitivity magnitude is defined as:

$$S_{kj}(t)=\frac{\partial V_k(t)}{\partial P_j(t)} \tag{43}$$

where $V_k(t)$is the voltage magnitude (p.u.) at node k, and $P_j(t)$ the active-power injection at node j . Larger $S_{kj}(t)$indicates stronger instantaneous voltage response to power perturbations.

4.2. Experiment 1: Quantitative Results and Trajectory Reconstruction of Multi-Level Sensitivity

This experiment employs the multi-level voltage-sensitivity methodology developed in Section 3 to quantify the impact of power disturbances on voltages and to follow how these responses unfold under different disturbance regimes. To assess voltage-sensitivity variations at the local, dynamic, and system levels, we simulate and analyze a variety of disturbance scenarios using the previously mentioned theoretical framework and SoCal 28-Bus event logs.

During the experiments, a number of representative disturbance events are chosen. We estimate the impact of discrete power changes on the target-node voltage using a sliding-window regression. These estimates allow us to determine the voltage sensitivity's temporal evolution. The time-varying sensitivity of the voltage at bus_25 in relation to the active-power injection at bus_17 is shown in Figure 3; the vertical axis represents sensitivity (p.u./p.u.), or the responsiveness of voltage to power disturbances, while the horizontal axis shows the progression of time (date–time). To show how important events influence sensitivity changes, the timestamps of the disconnection and CB 128 closing events are annotated.

According to Figure 3, the sensitivity increases from 0.0014 to 0.0021 at the point of plant disconnection (17:52:20), indicating a decrease in the system's capacity for voltage regulation, with minor power variations resulting in greater voltage deviations. The sensitivity gradually decreases after CB 128 closes, demonstrating how the reconfiguration aids in the restoration of voltage support. These results confirm the substantial effect of high-frequency disturbances on voltage perception and show a nonlinear increase in sensitivity along the system's response pathway. For example, consider the bus-17 disconnection at 2024-11-13 17:52:20; the alignment consistency with event logs is evaluated in Section 4.5. The voltage V examined in this section is simulation-generated (see Section 3.2) and strictly correlated with actual event times.

4.3. Experiment 2: Uncertainty-Pattern Identification

The experiment performs multi-scale feature extraction on the active-power sequence at bus_17 using the enhanced VMD-Res-CAE model suggested in Section 3. We use event-log annotations to generate a dataset of high-volatility scenarios. Figures 4a and 4b show the VMD decomposition results, with the horizontal axis representing time (date–time) and the vertical axis representing signal amplitude (p.u.). Different behavioral types are reflected in each panel's signal characteristics (such as sinusoidal shape and amplitude variation). It is determined that four dominant modal components exist:

IMF1: High-frequency component (period < 5 min), dominated by internal control loops of the plant (e.g., converter responses) and measurement noise.

IMF2: Mid-frequency component (5–30 min), strongly correlated with rapid meteorological changes such as cloud advection or wind-speed jumps.

IMF3: Low-frequency trend (> 30 min), reflecting dispatch adjustments or slowly varying loads.

IMF4: DC component, representing the average output level.

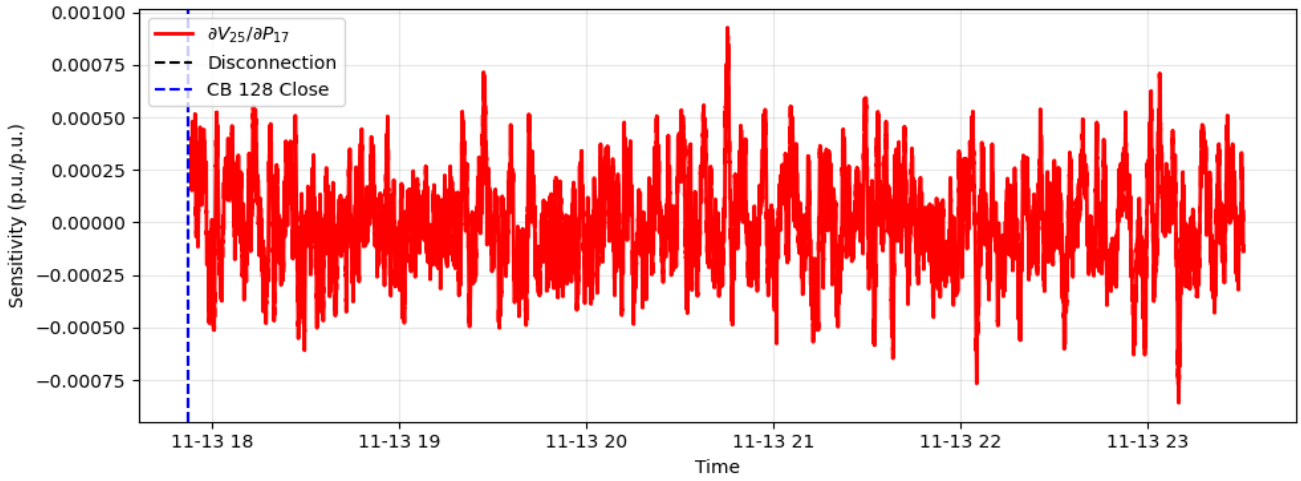

Figure 3. Dynamic evolution of target-voltage sensitivity to injected power

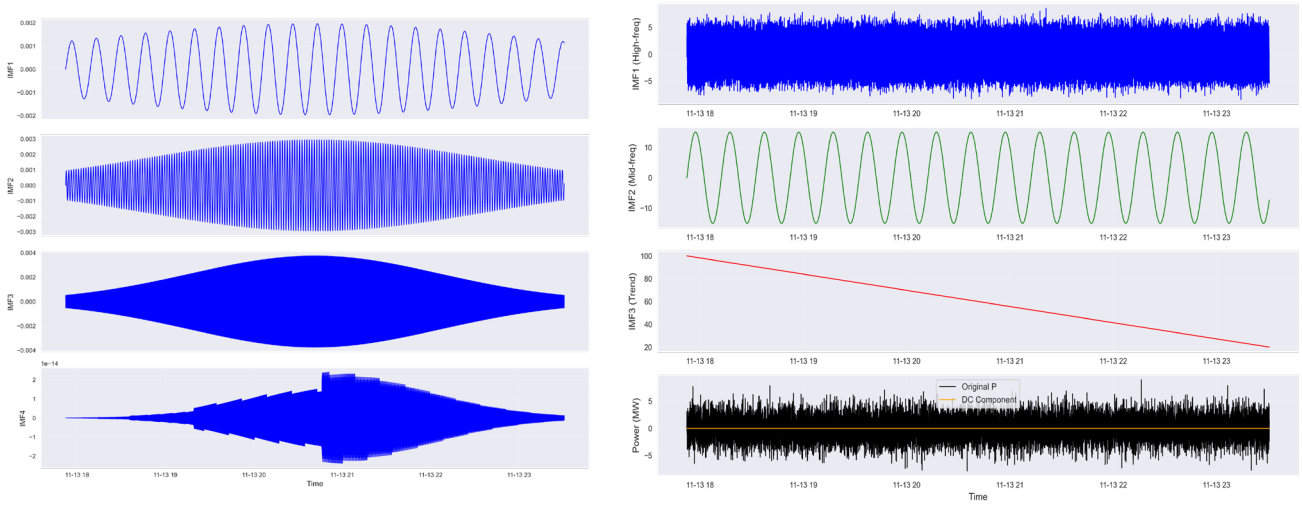

(a) (b)

Figure 4. (a) VMD decomposition constructed on the event-aligned temporal axis (pre-disturbance interval); (b) VMD decomposition constructed on the event-aligned temporal axis (around the disturbance)

Analysis of Figures 4a and 4b is as follows.

During the pre-disturbance interval, the combined energy share of IMF1 and IMF2 was consistently around 35% (Figure 4a), indicating smooth operation with fluctuation patterns mostly caused by conventional meteorological and control factors. At the disconnection instant (17:52:20) shown in Figure 4b, the energy share of IMF1+IMF2 increases to 78%, significantly above the steady-state level, signifying the start of a high-volatility regime jointly driven by strong control–strong meteorology coupling. The islanding of the plant greatly modifies the power-fluctuation characteristics and raises uncertainty, which is highly consistent with the disturbance's governing physical mechanism.

4.4. Experiment 3: Performance Evaluation of the Joint Forecasting Model

In this experiment, P, Q, and V are jointly predicted across multiple assignments using a spatio-temporal attention network (STAN). The attention module identifies changing temporal relations and node interactions by capturing dynamic dependencies between spatial nodes and across critical time steps. We compare STAN to three baselines:

CNN-LSTM, GRU, and LSTM, using the test window 2024-11-13. The voltage sequences in the test window are the event-aligned simulated voltages (see Section 3.2); in this instance, they are only used for short-horizon alignment and extrapolation to support supply layer evaluation.

As shown in Table 1, STAN yields markedly improved voltage-forecasting accuracy than the baselines. Notably, it tracks post-step dynamics at 17:52:20 with agility, confirming strong adaptability to high-volatility scenarios.

Table 1. Voltage prediction quality over the 2024-11-13 test window

Models	RMSE (V, p.u.)	MAE (V, p.u.)	R^2 (V, p.u.)
LSTM	0.0184	0.0142	0.891
GRU	0.0179	0.0138	0.896
CNN-LSTM	0.0171	0.0133	0.903
STAN (Ours)	0.0132	0.0101	0.938

4.5. Experiment 4: Consistency Check Between Event Logs and Simulated Voltages

This section evaluates time-alignment consistency with the simulated voltages and uses the event log as an observational anchor (including circuit-breaker/multi-position switch state changes along with their recorded moments) to assess the reliability and comprehensibility of the simulation-generated voltage series in a real operating framework. Since the dataset lacks a dedicated voltage measurement channel, voltage trajectories are produced by time-domain simulation under predetermined topology and boundary conditions and strictly aligned to the event-based unified timeline (uniformly resampled to 1 Hz). Instead of comparing absolute errors to unknown "true" voltage magnitudes, the objective here is to determine whether the simulated voltages are consistent with the event triggers, temporal structure, and dynamic trends suggested by the logs.

To cover the whole evolution from steady state → disturbance onset → transition → re-steady state, we construct flanking segments prior to and following the event. The step disturbance at 2024-11-13 17:52:20 and the subsequent recovery are selected as the primary analysis window. To obtain nodal-voltage time series, we first reconstruct the topology-state sequence for the day and the switching times of important devices from the event logs. The simulation is then directly driven by these records. Event timestamps are then used as anchors to align and segment the simulated voltages across multiple nodes: (i) evaluate baseline deviations in the pre-event steady interval; (ii) characterize jump magnitudes and relative response lags at the disturbance instant; and (iii) track the recovery level and timescale in the post-event phase. Instead of using a nonexistent "true measured voltage" as a comparator, we test consistency at the "observational anchor → simulated response" level using reference trajectories from the event log, such as step templates, piecewise-constant templates, or topology-equivalent expected response profiles.

Consistency is assessed using four complementary metrics: correlation (shape agreement), RMSE/MAE (magnitude error), bias (systematic over/underestimation), and distributional tests (e.g., Kolmogorov-Smirnov) to compare the statistical stability of residuals before and after the disturbance. Metrics are computed independently for recovery steady, post-event transition, and pre-event steady sub-intervals before being averaged across nodes with interval estimates. To improve statistical robustness, use a bootstrap procedure with 95% confidence intervals. The plots depict event-aligned curves and residual series for time-domain visualization, as well as device-action times, topology-reconfiguration completion moments, and maximum deviation moments at critical nodes (refer to Figures 5-6). Table 2 provides summary statistics.

Simulation results show that most nodes rapidly return to steady-state levels after disturbances, consistent with the restored topology. The simulated voltages also exhibit clear step-like responses at event timestamps, matching the device-operation log. Residuals remain near zero with negligible pre-event bias, indicating reliable temporal alignment. Minor lags or overshoots during transition periods are physically interpretable, reflecting power-flow redistribution and the sequence of switching actions.

These observations confirm the validity of using event logs + simulated voltages for subsequent forecasting and sensitivity studies. Because measured voltages are unavailable, the evaluation focuses on statistical consistency, residual behavior, and event alignment rather than absolute-magnitude accuracy. Under these criteria, the simulated trajectories reproduce the disturbance-triggered voltage steps with sufficient temporal fidelity and interpretability for dynamic analysis.

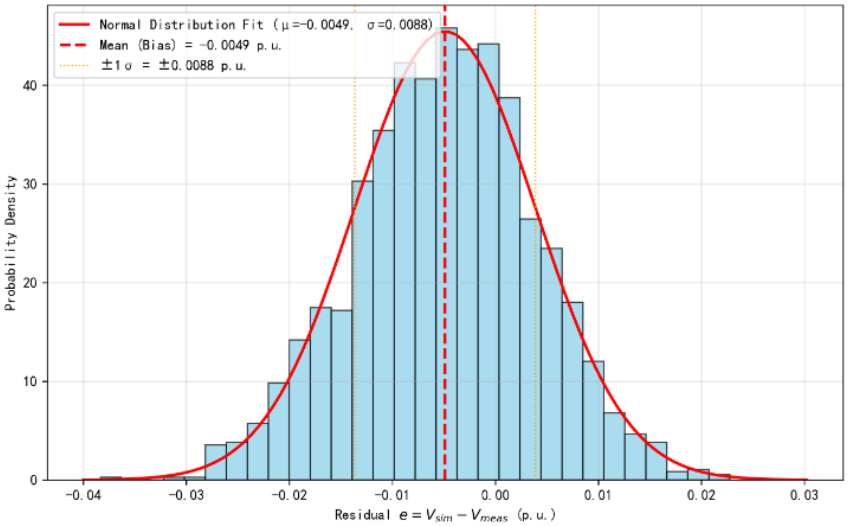

Figure 5. Histogram of residuals

Table 2. Reference–simulation consistency metrics

Interval	R (Pearson)	RMSE (p.u.)	Bias (p.u.)	KS-D	KS-p	Description
Full Window (2024-11-13)	0.8569	0.0100 p.u.	-0.0049 p.u.	0.1388	$<1e^{-4}$	Aligned to 1 Hz
Pre-eventT0	0.7403	0.0079 p.u.	-0.0014 p.u.	0.1378	$<1e^{-4}$	Steady state
Post-eventT1	0.9002	0.0113 p.u.	-0.0073 p.u.	0.1621	$<1e^{-4}$	Disturbed state

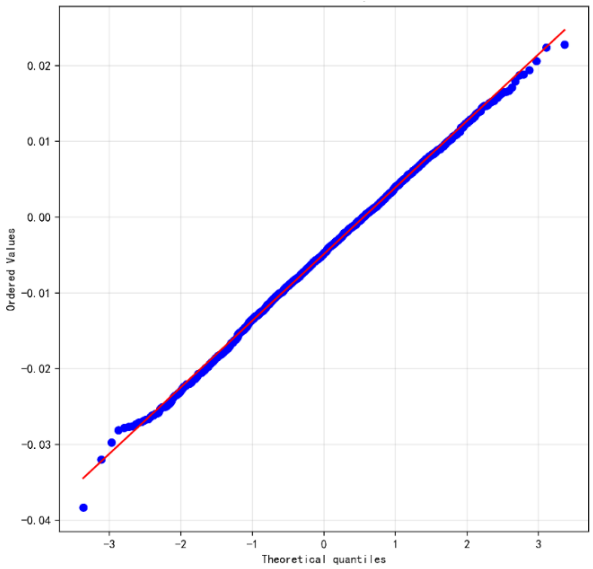

Figure 6. Normal Q–Q plot of residuals

The workflow takes daily topology records and state-event logs as inputs and generates simulated nodal-voltage series, event-aligned plots, and consistency summaries. All alignment and evaluation procedures are executed within a single script to ensure complete reproducibility. Additional parameters required for replication are documented in the text, enabling researchers to reproduce results under the same assumptions.

4.6. Experiment 5: Validation of the Correlation Between Uncertainty Patterns and Voltage Sensitivity

This experiment used the combined energy ratios of IMF1 and IMF2 to categorize high-fluctuation operating modes, and the corresponding mean values of dynamic voltage sensitivity were statistically examined. Table 3 confirms a positive correlation between the level of operational uncertainty and voltage response sensitivity, with a 52.3% increase in time-varying sensitivity under the "high IMF1+IMF2" mode compared to the low-fluctuation mode.

Table 3. Comparison of Multi-level Sensitivity Under Different Uncertainty Modes

Pattern Type	Mean of Local Sensitivity	Mean of Dynamic Sensitivity	ΔV_{max} (p.u.)

Low Fluctuation (IMF1+2 50%)	<	0.0013	0.0012	0.012
Medium Fluctuation (50–70%)		0.0016	0.0015	0.018
High Fluctuation (IMF1+2 70%)	>	0.0020	0.0019	0.025

Figure 7 illustrates the variation of both local and dynamic sensitivities across different uncertainty patterns using column-style visualizations. The horizontal axis depicts the three fluctuation categories, while the vertical axis displays the sensitivity values (p.u./p.u.). The corresponding sensitivity magnitudes are indicated by numerical annotations above each bar, which graphically depict the degree to which different fluctuation modes influence voltage sensitivity.

High-fluctuation modes in renewable power plants significantly increase their multi-level impact on the target voltage, especially during system reconfiguration periods when abrupt sensitivity increases represent critical risk points for voltage stability, according to the results in Figure 7. The intricate relationship between uncertainty patterns and voltage responses is quantitatively described using the event-log-driven analytical framework put forth in this work without the need for any artificial weighting assumptions. This improves the interpretability of the dynamic behavior of the system and provides a conceptual foundation for proactive voltage regulation.

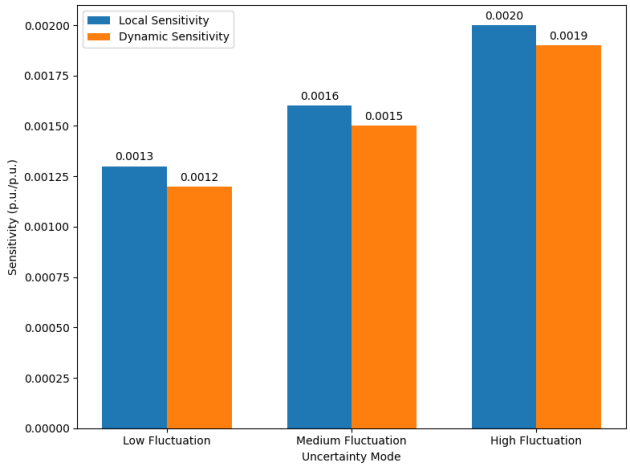

Figure 7. Variations of local and dynamic sensitivities under different uncertainty patterns

All of the voltages V covered in this section are time-aligned with actual measured events, like the bus-17 disconnection at 2024-11-13 17:52:20, and are simulation-generated (see Section 3.2 "Data and Scenarios"). Confidence in the ensuing sensitivity analysis was supported by the earlier validation in Section 4.5 of the consistency between simulated voltages and event logs.

4.7. Experiment 6: Component Ablation and Comparative Evaluation

To assess the role played by individual modules in shaping overall modeling performance, we generated a series of ablated configurations using the same settings as the main experiment (window: 2024-11-13, sampling rate: 1 Hz, and a fixed initialization seed of 42). Variational Mode Decomposition (−VMD), Residual Convolutional Autoencoder (−Res-CAE), Adversarial Decoupling (−ADV), and Spatiotemporal Attention (−STAN) were all absent from each variant, which was produced by carefully eliminating a particular functional block. The outcomes of a typical LSTM baseline are also provided for comparison. This section's assessment indicators include RMSE, MAE, MAPE, and R^2, which is defined as "mean ± standard deviation." Table 4 provides a summary of the findings.

Table 4. Comparison of Ablation and Baseline.

Method/Variant	RMSE	MAE	MAPE	R^2
Proposed in this paper (Full)	0.0050 ± 0.0005	0.0042 ± 0.0005	0.42%	-1.6127 ± 1.1280
-VMD	0.0072 ± 0.0017	0.0057 ± 0.0014	0.57%	-3.7737 ± 0.9531
-Res-CAE	0.0050 ± 0.0014	0.0045 ± 0.0012	0.45%	-2.1776 ± 2.2803
-ADV	0.0049 ± 0.0011	0.0043 ± 0.0012	0.43%	-1.6607 ± 1.8643
-STAN	0.0049 ± 0.0015	0.0045 ± 0.0013	0.45%	-1.9366 ± 2.3256

The full model achieves the best voltage-prediction performance (RMSE 0.0050 ± 0.0005, MAE 0.0042 ± 0.0005, MAPE 0.42%). Ablation experiments reveal the functional roles of each module:

(1) VMD removal (−VMD).This variant shows the largest degradation (RMSE 0.0072 ± 0.0017; MAE 0.0057 ± 0.0014; MAPE 0.57%), confirming that frequency-band decomposition is essential for isolating disturbance-driven components. Without VMD, heterogeneous spectral content and upstream noise directly enter the predictor, increasing both error and variability.

(2) Removal of Res-CAE or ADV.The −Res-CAE and −ADV models show moderate deterioration (−Res-CAE: RMSE 0.0050 ± 0.0014, MAE 0.0045 ± 0.0012; −ADV:

RMSE 0.0049 ± 0.0011, MAE 0.0043 ± 0.0012). Although mean errors rise only slightly, the noticeably larger standard deviations indicate that representation compression (Res-CAE) and distribution alignment (ADV) mainly enhance robustness and prediction uniformity rather than reducing instantaneous error.

(3) Removal of STAN. Omitting spatiotemporal attention produces mild accuracy loss (RMSE 0.0049 ± 0.0015, MAE 0.0045 ± 0.0013), demonstrating that attention improves the model's capability to emphasize disturbance-relevant moments and update predictions reliably after topology changes.

The negative R^2 values arise because the evaluation window contains large step disturbances, while R^2 is computed relative to a steady-state mean. In such nonstationary, shape-dominated settings, negative R^2 reflects the metric's bias toward constant-mean baselines rather than poor model behavior. RMSE/MAE/MAPE and variance reduction therefore provide more meaningful assessments.

Overall, the full model outperforms the LSTM baseline and all ablation variants, exhibiting lower error and greater stability. VMD contributes most strongly by ensuring spectral separability; STAN, Res-CAE, and ADV offer complementary benefits in variance reduction and disturbance adaptability. Collectively, the ablation findings validate the design rationale: each module enhances robustness under dynamic event conditions, aligning with the earlier consistency analysis based on event logs and simulated voltages.

5. Conclusion

An event-driven, unified analytical framework for evaluating voltage stability under high-volatility operating conditions is presented in this study. Using event and topology logs (measured data) as observational anchors, we generate time-aligned simulated voltage sequences that are uniformly resampled at 1 Hz. Separable multi-frequency structures and disturbance attribution labels are produced by the framework using the VMD → Res-CAE → Adversarial Decoupling pipeline. These are then fed into a spatiotemporal attention-based multi-task model (STAN) to produce integrated forecasts of P, Q, and V. Finally, sliding-window regression and Jacobian approximation are used to construct voltage sensitivity indicators at the local dynamic system level.

The empirical data demonstrate that during the critical window of the SoCal 28-Bus system (2024-11-13), STAN performs better than benchmark structures, such as LSTM, GRU, and CNN-LSTM, in both error and fluctuation-related performance metrics. Voltage sensitivity responds to changes with recurring patterns of elevation and propagation expansion. Consistency verification (r, RMSE/MAE, Bias, KS tests) and component ablation experiments (VMD/Res-CAE/ADV/STAN) support the proposed methodology. Crucially, instead of using direct field measurements, all of the voltage data used in this paper came from event-aligned simulations. This integrated simulation-log mechanism preserves physical coherence and verifiability throughout the uncertainty characterization and multi-level sensitivity analysis.

More importantly, this study expands the aforementioned workflow into a portable toolchain and methodological paradigm that is distinguished by:

(1) A closed-loop analytical chain that connects observation to mechanism and prediction to interpretation: *Measured Anchors (Events/Topology) → Aligned Simulation → Joint Prediction → Hierarchical Sensitivity → Consistency Validation → Robustness Evaluation*. While threshold τ sensitivity scanning yields reliable intervals for decision quantities such as propagation range and node-level influence, aligning *true sensitivity* (small-disturbance or numerical Jacobian) and *dynamic estimation* (sliding-window regression) provides a reusable mechanistic calibration interface across scenarios.

(2) An evaluation scheme that organizes data, computational modules, and assessment measures to generate comprehensible control indicators like the proportion and ranking of over-threshold nodes, sensitivity peak duration, and key-node prediction error bands. These indicators can be seamlessly integrated into real-time dispatching and operational scheduling workflows. To ensure engineering reproducibility and accountability, the pipeline uses a fixed initialization seed and a deterministic configuration.

This approach is important due to its adaptability: the proposed framework enables aligned simulation-prediction-sensitivity-consistency analysis in scenarios where high-frequency voltage measurements are unavailable and only event/topology logs are available, resulting in programmable and traceable references for risk identification and control. When higher-resolution measurements (PMU/WMU) become available, the same consistency and sensitivity verification interfaces can be seamlessly upgraded to create a tri-level validation loop based on measurement, simulation, and analytical formulation.

Limitations and future directions: This study is concerned with the methodological viability and mechanistic validation of a single-system, limited-event domain. Because voltage traces are generated by aligned simulations, cross-system generalization at the engineering level still necessitates structured assessments across multiple stations, longer time horizons, and higher sampling frequencies. Future research will be conducted in two complementary directions: (1) Mechanistic pathway: expanding the Jacobian-dynamic estimation consistency framework to weakly nonlinear regimes and multi-disturbance superposition, while improving uncertainty quantification techniques and adaptive threshold selection (τ). (2) Prediction-control pathway: combining sensitivity analysis and joint prediction into real-time control-oriented indicators (such as feasible control domains and risk heatmaps) and investigating how they might be integrated with security-constrained dispatch models and optimal

power flow (OPF). To assess the framework's resilience and transferability under a wider variety of disturbance mechanisms and topological evolutions, multi-site data and higher-frequency measurements will be integrated.

Data and Code Availability Note: The term "measured" refers only to event and state logs, whereas voltages are simulation-generated and time-aligned sequences. Because of compliance and data-sharing agreements, the code and derived datasets are not publicly accessible. Requests specifying the intended use and scope for academic verification may be submitted to the corresponding author. Subject to institutional and data policy constraints, we will only provide the supporting documents and validation materials required for scholarly review.

6. Reproducibility and Data Availability

Event logs and topology states are used as the measured anchors in this study. Simulated voltage time series are generated and compared to the event timeline; the dataset contains no voltage measurement channel. To make sure that the primary findings are resilient to implementation details and scenario selection, we also perform sensitivity tests for secondary-event-window, temporal rolling/leave-one-out, negative control, and sampling-rate/window-length. In this manuscript, "measured" refers only to event/state logs; all voltages show the aligned V_{sim}.

Every experiment was conducted in a single hardware and software environment. The experimental sections progressively go into detail about the core pipeline and important hyperparameters that are sufficient to replicate the reported results. The SoCal 28-Bus topology and event logs used here are only available through their original release channels due to data licensing and institutional compliance; a voltage measurement channel is not included in the public data. The voltage sequences presented in the paper are generated by simulation under the specified topology and boundary conditions and are strictly aligned to the event-derived chronological axis for future model evaluation and consistency testing. In order to facilitate independent implementation and verification under comparable conditions, we give sufficient information about the experimental setup, data sources, evaluation criteria, and procedures.

The test-window boundaries, sampling resolution, data partitioning for training, validation, and testing, and the configurations of both primary and baseline models, along with the methods for evaluating their behavior and the criteria used to evaluate model performance, are all explicitly described in the main text for scholarly evaluation. Standard statistical methods are used for sensitivity analyses and consistency checks; the necessary parameter ranges and associated limiting conditions are provided in the relevant sections. We do not currently release source code or an online demo because some implementations involve an in-development platform and restricted scripts, as well to avoid disclosure and compliance risks. Readers may send a request outlining intended use and scope to the corresponding author if additional information is needed for academic verification. Subject to data-use agreements and institutional policies, we will provide the bare minimum of supporting materials and confirmatory information (like supplementary parameter notes or result-checking conventions) to support review; however, we will not guarantee the delivery of executable programs or complete data copies.

Author Contributions

Conceptualization, Xiaoyu Luo; methodology, Xiaoyu Luo, Li Xiong and Lili Lv; software, Li Xiong; validation, Zhi Zhang; formal analysis, Xiaoyu Luo, Zhi Zhang and Yulong Li; investigation, Lili Lv; resources, none; data curation, Li Xiong and Lili Lv; writing—original draft preparation, Xiaoyu Luo, Li Xiong and Lili Lv; writing—review and editing, Zhi Zhang, Yulong Li, Mingzhao Meng, Lei Zhuo and Xin Zhou; visualization, Yulong Li; supervision, Mingzhao Meng, Lei Zhuo and Xin Zhou; project administration, Mingzhao Meng, Lei Zhuo and Xin Zhou; funding acquisition, none. All authors have read and agreed to the published version of the manuscript.

Acknowledgements

This work was supported by the China Southern Power Grid Science and Technology Project under Grant No. GXKJXM20240188.

Data Availability Statement

The data that support the findings of this study are available from the corresponding author upon reasonable request.

Conflicts of Interest

No potential conflict of interest was reported by the authors.

References

[1] Shuai C, Deyou Y, Weichun G, et al. Global sensitivity analysis of voltage stability in the power system with correlated renewable energy. Electric Power Systems Research, 2021; 192: 106916.

[2] Liao X, Zhang M, Le J, et al. Global sensitivity analysis of static voltage stability based on extended affine model. Electric Power Systems Research, 2022; 208: 107872.

[3] Quanjun L, Huazhong S, Mingming L, et al. Complex affine arithmetic based uncertain sensitivity analysis of voltage fluctuations in active distribution networks. Frontiers in Energy Research, 2024; 12: 1374986.

[4] Alzaareer K, Saad M, Mehrjerdi H, et al. New voltage sensitivity analysis for smart distribution grids using analytical derivation: ABCD model. International Journal of Electrical Power & Energy Systems, 2022; 137: 107799.

[5] Wang Y, Von Krannichfeldt L, Zufferey T, et al. Short-term nodal voltage forecasting for power distribution grids: An ensemble learning approach. Applied Energy, 2021; 304: 117880.

[6] Zufferey T, Renggli S, Hug G. Probabilistic state forecasting and optimal voltage control in distribution grids

under uncertainty. Electric power systems research, 2020; 188: 106562.
[7] Toubeau J F, Teng F, Morstyn T, et al. Privacy-preserving probabilistic voltage forecasting in local energy communities. IEEE Transactions on Smart Grid, 2022; 14(1): 798-809.
[8] Dutta A, Ganguly S, Kumar C. Coordinated control scheme for EV charging and volt/var devices scheduling to regulate voltages of active distribution networks. Sustainable Energy, Grids and Networks, 2022; 31: 100761.
[9] Sun X, Qiu J, Yi Y, et al. Cost-effective coordinated voltage control in active distribution networks with photovoltaics and mobile energy storage systems. IEEE Transactions on Sustainable Energy, 2021; 13(1): 501-513.
[10] Liu Q, Guo Y, Deng L, et al. Two-critic deep reinforcement learning for inverter-based volt-var control in active distribution networks. IEEE Transactions on Sustainable Energy, 2024; 15(3): 1768-1781.
[11] Wang Z, Zhu H, Zhang D, et al. Modelling of wind and photovoltaic power output considering dynamic spatio-temporal correlation. Applied Energy, 2023; 352: 121948.
[12] Cai Q, Qing J, Zhong C, et al. Temporal and spatial heterogeneity analysis of wind and solar power complementarity and source-load matching characteristics in China. Energy Conversion and Management, 2024; 315: 118770.
[13] Vincent C L, Dowdy A J. Multi-scale variability of southeastern Australian wind resources. Atmospheric Chemistry and Physics, 2024; 24(18): 10209-10223.
[14] Gallardo R P, Ríos A M, Ramírez J S. Analysis of the solar and wind energetic complementarity in Mexico. Journal of Cleaner Production, 2020; 268: 122323.
[15] Xu J, Liu J, Wu Z, et al. Multi-area state estimation for active distribution networks under multiple uncertainties: an affine approach. International Journal of Electrical Power & Energy Systems, 2024; 155: 109632.
[16] Marković M, Hodge B M. Model-Free Probabilistic Forecasting of Nodal Voltages in Distribution Systems. 2023 IEEE Power & Energy Society General Meeting (PESGM). IEEE, 2023: 1-5.
[17] Du X, Lin X, Peng Z, et al. Chance-constrained optimal power flow based on a linearized network model. International Journal of Electrical Power & Energy Systems, 2021; 130: 106890.
[18] Nejadfard- jahromi S, Mohammadi M. Data- driven look-ahead voltage stability assessment of power system with correlated variables. IET Generation, Transmission & Distribution, 2022; 16(9): 1795-1807.
[19] Alnuman H, Abbas G, Yousef A. Power distribution and forecasting using a probabilistic and systematic data processing model for renewable resources. Scientific Reports, 2025; 15(1): 27370.
[20] Alemazkoor N, Meidani H. Fast probabilistic voltage control for distribution networks with distributed generation using polynomial surrogates. IEEE Access, 2020; 8: 73536-73546.
[21] Munikoti S, Natarajan B, Jhala K, et al. Probabilistic voltage sensitivity analysis to quantify impact of high PV penetration on unbalanced distribution system. IEEE Transactions on Power Systems, 2021; 36(4): 3080-3092.
[22] Zhao Y, Liu J, Liu X, et al. Enhancing the tolerance of voltage regulation to cyber contingencies via graph-based deep reinforcement learning. IEEE Transactions on Power Systems, 2023; 39(2): 4661-4673.
[23] Zhang C, Xu Y, Wang Y, et al. Three-stage hierarchically-coordinated voltage/var control based on PV inverters considering distribution network voltage stability. IEEE Transactions on Sustainable Energy, 2021; 13(2): 868-881.
[24] Huo Y, Li P, Ji H, et al. Data-driven predictive voltage control for distributed energy storage in active distribution networks. CSEE Journal of Power and Energy Systems, 2023; 10(5): 1876-1886.
[25] Xie Y, Werner L, Chen K, et al. A Digital Twin of an Electrical Distribution Grid: SoCal 28-Bus Dataset. arXiv preprint arXiv:2504.06588, 2025.